Simulation of patient-specific bidirectional pulsating nasal aerosol dispersion and deposition with clockwise 45° and 90° nosepieces

Ali Farnoud, Ingo Baumann, Mohammad Mehdi Rashidi, Otmar Schmid, Eva Gutheil

PII: S0010-4825(20)30182-7

DOI: https://doi.org/10.1016/j.compbiomed.2020.103816

Reference: CBM 103816

To appear in: *Computers in Biology and Medicine*

Received Date: 30 April 2020

Revised Date: 5 May 2020

Accepted Date: 8 May 2020

Please cite this article as: A. Farnoud, I. Baumann, M.M. Rashidi, O. Schmid, E. Gutheil, Simulation of patient-specific bidirectional pulsating nasal aerosol dispersion and deposition with clockwise 45° and 90° nosepieces, *Computers in Biology and Medicine*, https://doi.org/10.1016/j.compbiomed.2020.103816.

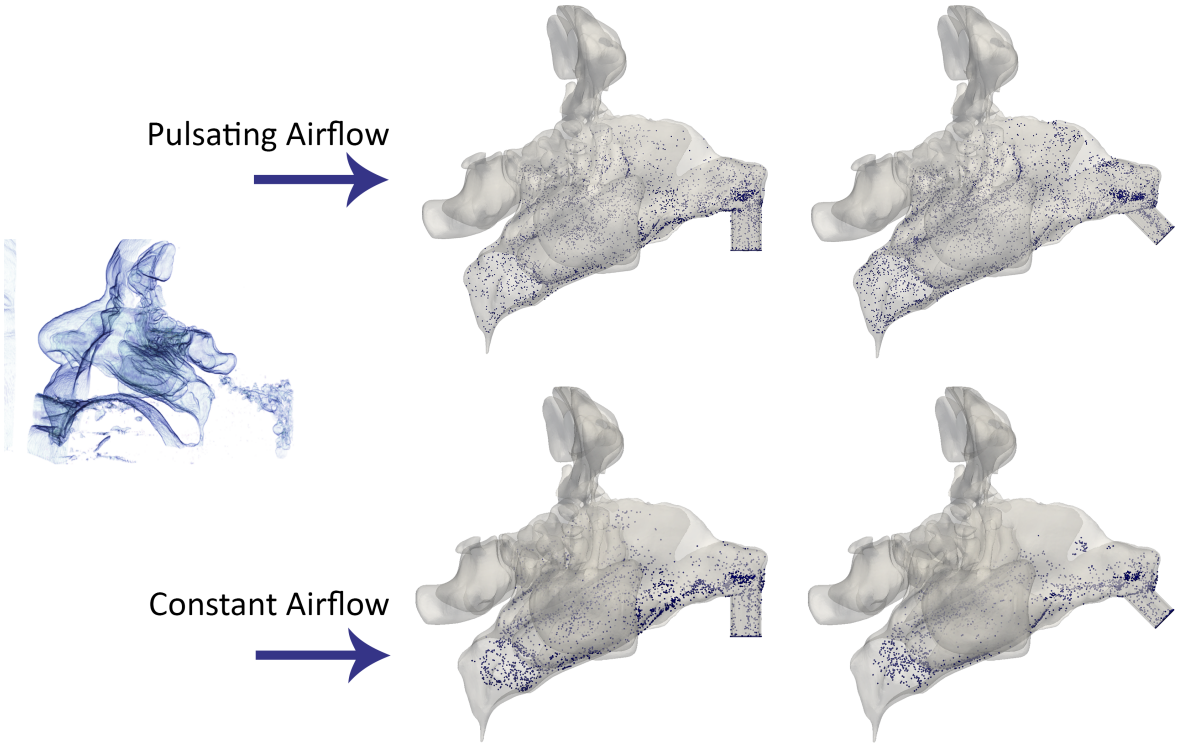

Simulation of Patient-Specific Bidirectional Pulsating Nasal Aerosol Dispersion and Deposition with Clockwise 45° and 90° Nosepieces

Ali Farnoud [a, b, e*], *Ingo Baumann* [c], *Mohammad Mehdi Rashidi* [d*], *Otmar Schmid* [a, b], *Eva Gutheil* [e]

[a] *Comprehensive Pneumology Center, Member of the German Center for Lung Research, Max-Lebsche-Platz 31, 81377 Munich, Germany*

[b] *Institute of Lung Biology and Disease, Helmholtz Zentrum München, 85764 Neuherberg, Germany*

[c] *Department of Otorhinolaryngology, Head and Neck Surgery, Medical Center of Heidelberg University, Heidelberg, Germany*

[d] *Institute of Fundamental and Frontier Sciences, University of Electronics and Technology of China, Chengdu 610054, Sichuan, P. R. China*

[e] *Interdisciplinary Center for Scientific Computing, Heidelberg University, Heidelberg, Germany*

[*] Corresponding author: mm_rashidi@yahoo.com, alifarnod@gmail.com

Abstract

Numerical simulations of the dispersion and deposition of poly-disperse particles in a patient-specific human nasal configuration are performed. Computed tomography (CT) images are used to create a realistic configuration of the nasal cavity and paranasal sinuses. The OpenFOAM software is used to perform unsteady Large Eddy Simulations (LES) with the dynamic sub-grid scale Smagorinsky model. For the numerical analysis of the particle motion, a Lagrangian particle tracking method is implemented. Two different nosepieces with clockwise inclinations of 45° and 90° with respect to the horizontal axis are connected to the nostrils. A sinusoidal pulsating airflow profile with a frequency of 45 Hz is imposed on the airflow which carries the particles. Flow partition analysis inside the sinuses show that ventilation of the sinuses is improved slightly when the 45° nosepiece is used instead of the 90° nosepiece. The flow partition into the right maxillary is improved from 0.22 % to 0.25 %. It is observed that a closed soft palate increases the aerosol deposition efficiency (DE) in the nasal cavity as compared to an open soft palate condition. The utilization of pulsating inflow leads to more uniform deposition pattern in the nasal airway and enhances the DE by 160 % and 44.6 %, respectively, for the cases with clockwise 45° and 90° nosepieces, respectively. The bi-directional pulsating drug delivery with the same particle size distribution and inflow rates as the PARI SINUS device result in higher total DEs with 45° nosepiece than with the 90°. Thus, the numerical simulation suggests the 45° nosepiece is favorable in terms of the delivered dose.

Keywords: Bi-directional aerosol delivery; Pulsating drug delivery; Nasal cavity; Computational fluid dynamics

1. Introduction

The inner cavity of the nasal airway located at the upper respiratory system is a geometrically complex structure which can be accessed via two nostrils. The cavity is separated into the left and right parts by the nasal septum which are not necessarily symmetric. The main nasal passage is divided into different regions such as vestibule, olfactory, and respiratory. The vestibule resides at the anterior part of the nose airway and it ends at the narrow and constricted region of the airway called nasal valve. The cross-sectional area of the nasal cavity significantly increases after the nasal valve, this section is known as respiratory region. Three meatuses

(inferior, middle, and superior) are located in the respiratory region and are lined with pseudostratified ciliated columnar epithelial cells [1]. The main nasal airway is surrounded by maxillary, ethmoid, frontal, and sphenoid sinuses that are air-filled bony cavities.

The nasal airway is a potential path for drug delivery to treat various diseases and became a growing field of study for pharmaceutical delivery [2]. Traditional nasal drug delivery leads to deposition of particles mainly in the frontal parts or nasopharynx due to inertial impaction and posterior regions of the nasal airway are not accessible [3]. However, novel nebulizers generate smaller particles with a mass median diameter (MMD) of less than 5 µm [4] and, in comparison to nasal sprays, lead to a more uniform deposition of the particles in the nasal airway. In several in-vitro [5-8] and in-vivo [9-12] studies, the airflow and particle dispersion and deposition pattern in human nasal cavity was investigated. Due to the time consumption and technical difficulties of in-vivo and in-vitro experiments, computational fluid dynamic (CFD) is an alternative to assess the airflow and particle pattern in the human nasal cavity.

The early CFD studies on the airflow profile in the realistic nasal cavity were performed by Keyhani et al. [13] and Subramaniam et al. [14] for low inlet flow rates. Inthavong et al. [15] evaluated the influence of the angle of the nasal spray with the nostril on the deposition efficiency of the particles. The connection angle was described as the angle of the nasal spray with the horizontal plane from the sagittal view (counter-clockwise). For particles in the micron-size range of 10 µm to 15 µm with uniform injection at the inlet cross section, the highest deposition efficiency (DE) in the anterior region occurred with the insertion angle of 100° whereas the lowest DE at the frontal region was found with the insertion angle of 70°. For the particles with diameters of 20 µm, the minimum DE occurred when the insertion angle of 45° was used which means that more particles move to the posterior parts. Numerical simulations show that high airflow rates and large particles cause higher particle deposition efficiencies in the nasal valve and the anterior regions of the nasal cavity [16, 17]. Shi et al. [18] found that particles with diameters between 1 µm and 50 µm carried by flow rates of 7.5 L/min to 20 L/min scarcely deposit in the inferior and olfactory regions due to the anatomical complexity of the nasal cavity. Shi et al. [19] showed that approximately half of a percent of the total amount of administered nanoparticles deposit in the olfactory region [20]. Moreover, Shi et al. [20] found that particle trajectory is significantly affected by turbulent dispersion. Covello et al. [21] used large eddy simulation (LES) for thermal water transportation inside the nasal cavity for the treatment of inflammatory disorders. Calmet et al. [22] resolved all the spatial and temporal scales of the airflow in the human cavity during a rapid inhalation and concluded that a very fine volume grid was required to capture the transitional features in the nasal cavity. Calmet et al. [23] used three patient-specific nasal cavities to analyze the dispersion and deposition of microparticles carried by low-to-medium flow rates. The regional deposition of

the particles for three patients were very different for the particle diameters of 2 µm, 10 µm, and 20 µm.

Innovative techniques have been developed to improve the distribution and deposition of the particles inside the nasal airway during the drug delivery process. OptiNose US Inc. developed a bi-directional nasal drug delivery system that increases DE in the nasal airway. The individual exhales into the mouthpiece and the device injects the particles into the nasal cavity through nostrils. By exhaling into the pipe which is connected to the mouth, the connection between the nose and throat is closed by the upwards movement of the soft palate. Therefore, the particles enter through one side of the nasal airway and exit through the other side of the nasal cavity [24, 25]. Kleven et al. [26] studied the bi-directional drug delivery with the PARI SINUS nebulizer using the flow rate of 6 L/min and particles with mean diameters of 3.5 µm which showed a total DE of 63.1 ± 18.4% in nasal cavity. They also simulated the DE of monodisperse particles during bi-directional delivery and found that the DE is underestimated with computational models simulated by Ansys Fluent.

Frank et al. [27] detected that after the surgery, the deposition of the particles with sizes between 10 µm and 110 µm in the anterior regions decreased by 13 %. The post-surgery results depicted that the deposition of the particles in the posterior regions increased by 118 %. Furthermore, latest studies suggest that the generation of a pulsating airflow as a carrier phase improves the ventilation of air in the meatuses that are connected to paranasal sinuses via ostia [9, 11, 12, 28-30]. Xi et al. [31] experimentally obtained a relation between the dosage inside the nasal sinuses and the ostium diameter. Moreover, they numerically depicted that the maximum deposition in sinuses occur when the airflow with pulsating frequency equal to the resonance frequency is used which is dependent on the ostium and sinus geometry and independent of the main nasal cavity geometry. Xi et al. [32] developed an electric-guided delivery system which led to higher osteomeatal complex dose than standard nasal devices. Xi et al. [33] concluded from their experimental and numerical study that the implementation of bi-directional nasal drug delivery enhances the ventilation of the upper parts of the nasal cavity. Furthermore, Xi et al. [34] experimentally studied DEs for the open soft palate and closed soft palate conditions and reported that DE of 24 ± 6 % for the bi-directional drug delivery with pulsating inlet airflow rate of 6 L/min. Their results showed a two-fold enhancement in DE with the utilization of the bi-directional drug delivery technique compared to the normal nasal drug delivery. Möller et al. [11] evaluated the ventilation of airflow and particles in three healthy volunteers by utilization of non-pulsating and pulsating flows with a frequency 45 Hz which showed DEs of 58 ± 17 % and 25 ± 16 % with pulsating and non-pulsating airflow of the PARI SINUS device. Leclerc et al. [35] studied the effect of different nebulization conditions such as non-pulsating and pulsating aerosol delivery with a frequency of 90 Hz with both micro- and nanoparticle injections. They found that more particles deposit inside maxillary sinuses by

utilization of nanoparticles and pulsating aerosol delivery with a frequency of 90 Hz. Farnoud et al. [36] compared two pulsating flow conditions in the main nasal airway where the connection of the nasal cavity and the pharynx was open. They compared the constant and dynamic Smagorinsky turbulence models and their effects on the ventilation of the air in the nasal cavity. Moreover, they assessed the influence of one-way and two-way coupling between the gas phase and the mono-disperse particles which showed a higher DE when two-way coupling was implemented. However, in their study, the sinusoidal pulse was simplified. The particle deposition pattern in the nasal cavity is not uniform and particles mainly deposit in the nasal valve and nasopharynx and the lower parts of the cavity, resulting in very low access of the particles in the olfactory region, middle and superior meatuses, and posterior regions of the nasal cavity.

The present numerical investigation focuses on the effect of clockwise 45° and 90° nosepieces during bi-directional pulsating aerosol on particle dispersion and deposition, and the resulting deposition pattern is compared to that of the particle deposition of an equivalent non-pulsating inlet airflow.

2. Methodology

A workflow is developed which starts from segmented CT images and subsequent reconstruction of the three-dimensional geometry using 3DSlicer, see Fig. 1. The ICEM-CFD Ansys was used for generating a tetrahedral mesh with three layers of a prism mesh. Then the generated mesh was imported into OpenFOAM for the numerical simulation. The Euler-Lagrange formulation was implemented for simulating the fluid flow and the motion of poly-disperse particles in the patient-specific nasal airway including the non-ventilated paranasal sinuses. A two-phase approach was used for considering air and particles interaction.

The three-dimensional, intricate geometry of the nasal airway is reconstructed from the sequence of CT images taken on an 80 years old male patient airway. The CT images have a slice thickness of 1 mm, the resolution is 2.32 pixels per mm, and the pixel size is 0.4297×0.4297 mm^2. Figure 2 illustrates the CT images of the patient which depict a slight septum deviation to the left and healthy inferior, middle, and superior meatuses. All of the paranasal sinuses are healthy and the diameters of the left and the right ostia are 4.58 mm and 5.45 mm, respectively. The length of the nasal cavity is 9.9 cm. It should be mentioned that nasal cycling causes more congestion in one side of nasal cavity compared to the other side which could add some uncertainties to the model [37]. In order to create a bi-directional drug delivery condition, the patient was asked to keep a pipe in his mouth during the imaging procedure, see Fig. 3. Therefore, the soft palate closes the connection of the nasal airway and the pharynx, and the airflow and the particles enter the nasal airway through one nostril and

move out of the nasal passage through the other nostril. The airflow and the particles change their direction by 180° in the nasopharynx region, see Fig. 4.

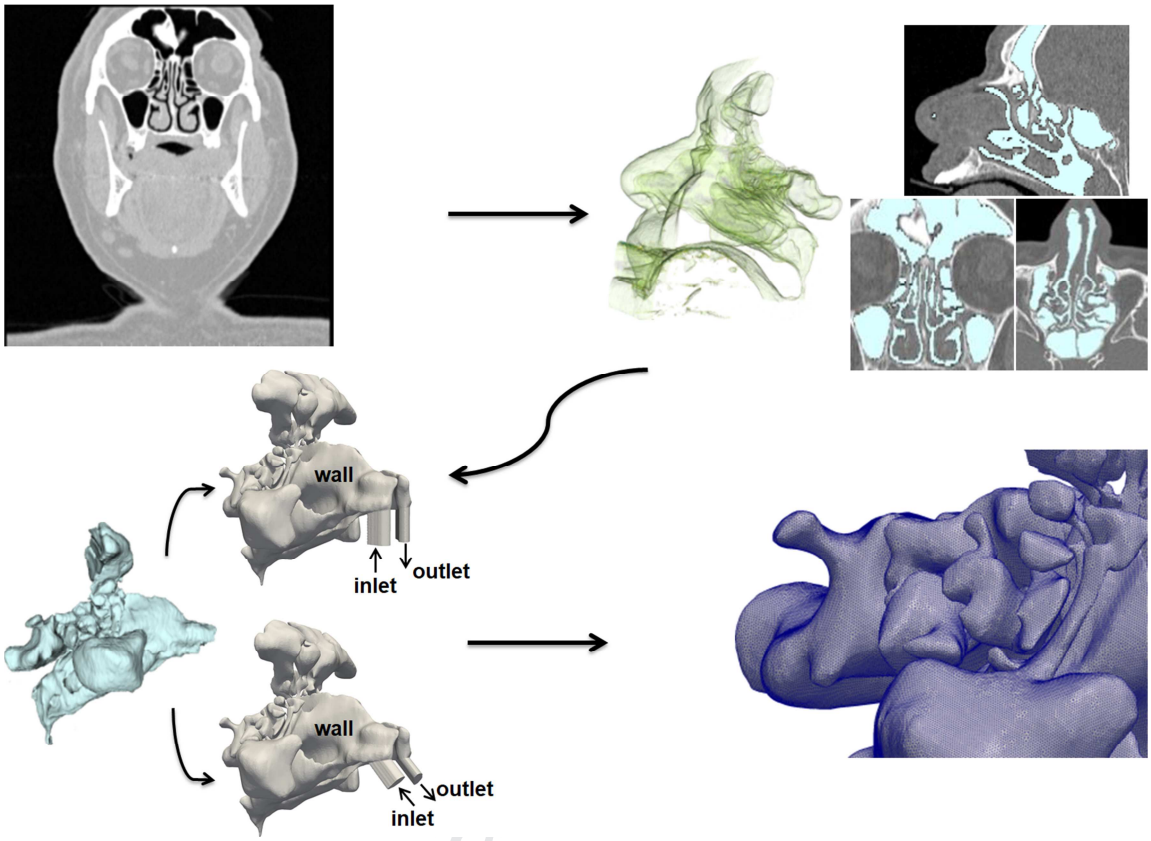

Figure 1. The workflow from CT images to the surface and volume grid cells in a patient-specific nasal cavity.

The CT images originally are in DICOM format and they are processed in 3DSlicer [38] where the region of interest is identified and artifacts due to filled teeth of the patient are removed. Furthermore, the nasal cavity is reconstructed by recommended thresholding in Hounsfield units for air segmentation by experts, and the STL file was extracted using 3DSlicer [38]. Due to very high surface roughness and holes in the segmented geometry which is not suitable for CFD simulations, further smoothing and improvement on the surface resulting in smaller holes are performed with the software package Blender [39] and a new STL file is extracted. The STL data file is imported into the commercial software ICEM-CFD Ansys, and the extension pipes at the nostrils are added to the geometry. Two different nosepieces are connected to the nostrils with clockwise inclinations of 90° and 45° with respect to the horizontal plane, see Fig. 4, where the workflow from CT images to the mesh generation is depicted. For both geometries, approximately 20 million unstructured tetrahedral cells with three prism layers are generated as can be seen in Fig. 5.

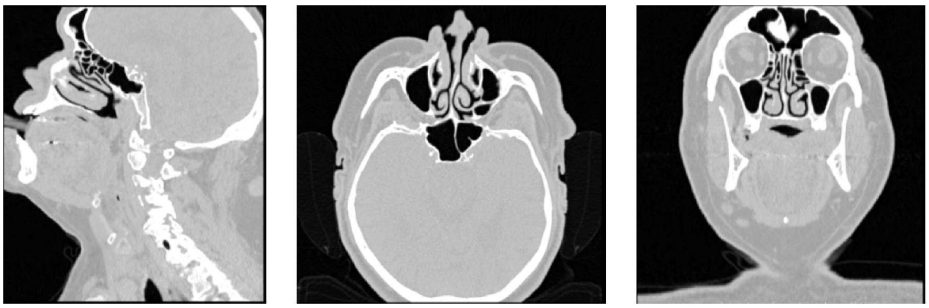

Figure 2. CT images from sagittal, axial, and coronal views (left to right) [36].

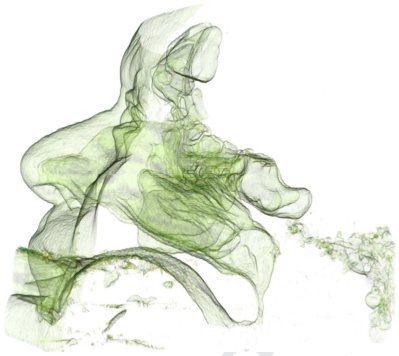

Figure 3. Closed soft palate condition by keeping the mouth open by a pipe.

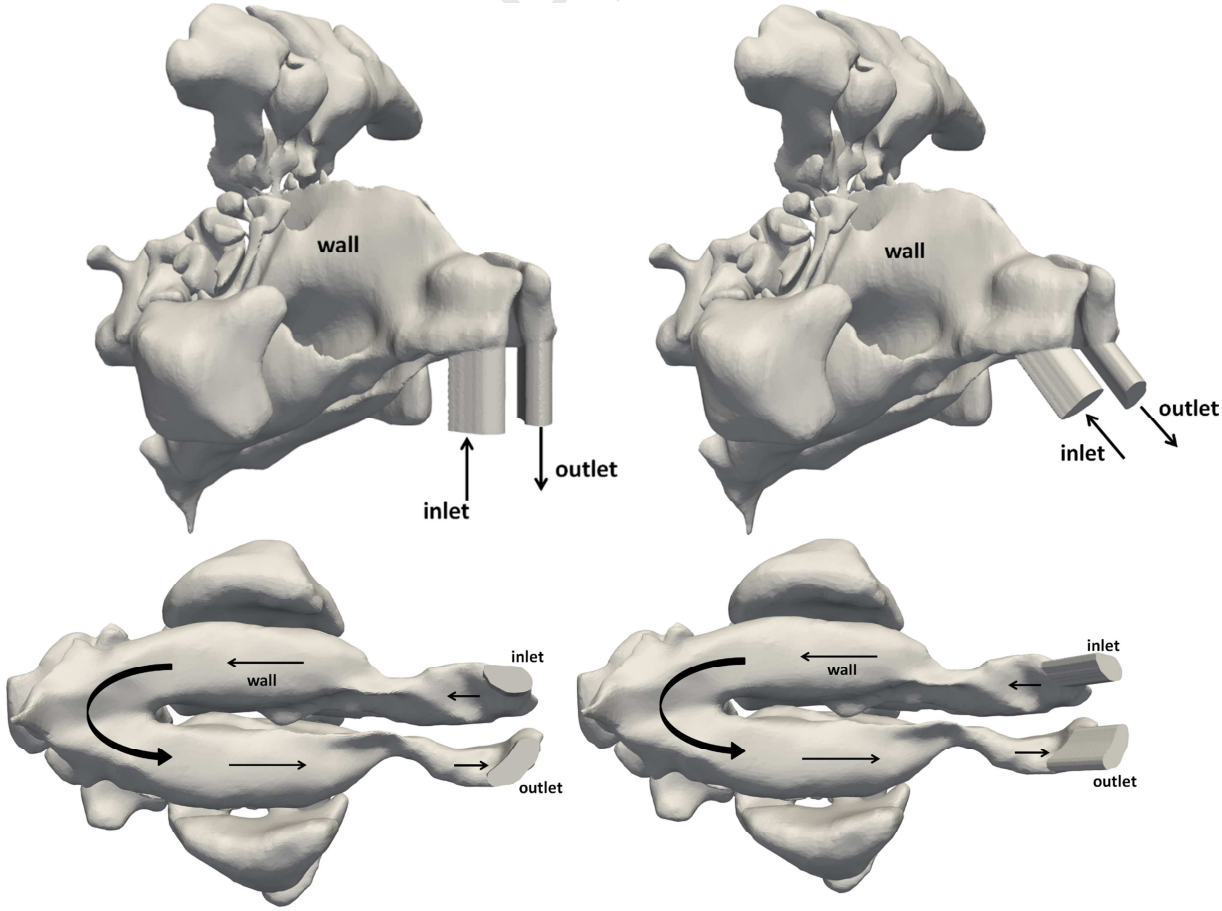

Figure 4. Geometry of the nasal cavity including all paranasal sinuses with clockwise 90° (left) and 45° (right) nosepieces.

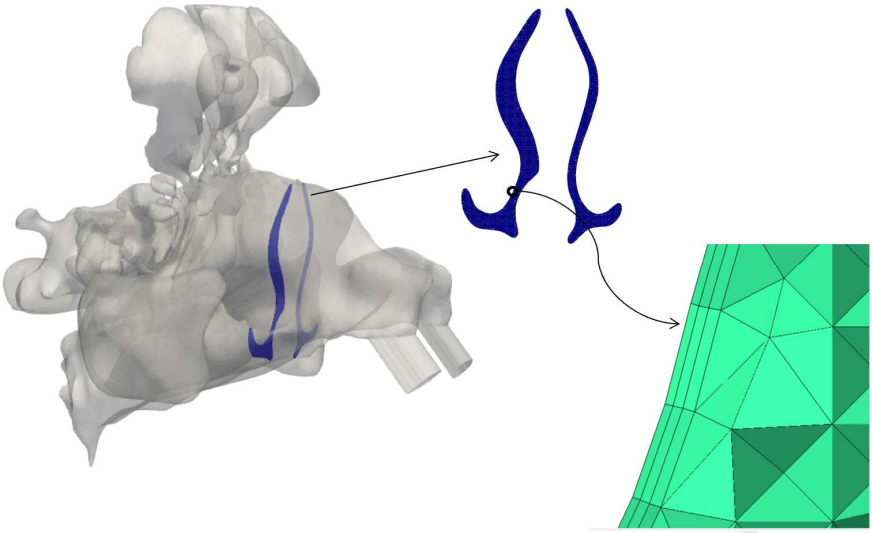

Figure 5. Geometry and the generated mesh from different views.

2.1.Governing Equations

Three-dimensional, incompressible unsteady Navier-Stokes equations are numerically solved for isothermal condition. A LES turbulence model [40] is implemented for simulating the fluid flow which may be laminar, transitional, or turbulent. Furthermore, a two-phase flow model was used for considering the interaction between air-flow and particles [41]. In the constant Smagorinsky sub-grid scale (SGS) model, the grid filter width of $\bar{\Delta}$ is implemented in the continuity and the momentum equations as

$$\bar{f}(x) = \int f(x')\bar{G}(x,x')dx' \quad (1)$$

Using an eddy viscosity hypothesis, the sub-grid stress tensor τ_{ij}^{r} yields [42]

$$\tau_{ij}^{r} - \left(\frac{\delta_{ij}}{3}\right)\tau_{kk}^{r} \approx -2\vartheta_r \overline{S_{ıȷ}} \quad (2)$$

Moreover, by implementation of the Smagorinsky coefficient C_s, the eddy viscosity is closed, $\vartheta_r = (C_s\bar{\Delta})^2|\bar{S}|$, $\overline{S_{ıȷ}} = 1/2(\frac{\partial \overline{U_ı}}{\partial x_j} + \frac{\partial \overline{U_ȷ}}{\partial x_i})$ and $|\bar{S}| = (\overline{S_{ıȷ}}\,\overline{S_{ıȷ}})^{1/2}$ [42], leading to

$$\tau_{ij}^{r} - \left(\frac{\delta_{ij}}{3}\right)\tau_{kk}^{r} \approx -2C_s\bar{\Delta}^{\,2}|\bar{S}|\overline{S_{ıȷ}} \quad (3)$$

For the dynamic SGS model, the filtered equations are exposed to another so-called test filter with filter width $\tilde{\Delta}$

$$\tilde{f}(x) = \int f(x')\tilde{G}(x,x')dx' \quad (4)$$

leading to double-filtered equations where the bar denotes the grid filter and the tilde the test filter due to the Smagorinsky SGS model. Thus, the governing equations for mass and momentum result in

$$\frac{\partial \widetilde{\overline{U_j}}}{\partial x_j} = 0 \tag{5}$$

$$\frac{\partial \widetilde{\overline{U_i}}}{\partial t} = -\frac{\partial(\widetilde{\overline{U_i}}\,\widetilde{\overline{U_j}})}{\partial x_j} - \frac{\partial \tilde{\bar{p}}}{\partial x_i} - \frac{\partial T_{ij}}{\partial x_j} + \frac{1}{\mathrm{Re}}\frac{\partial^2 \widetilde{\overline{U_i}}}{\partial x_j x_j} + \widetilde{\overline{S_{\mathrm{p},i}}} \tag{6}$$

In equations (5) and (6), the Einstein summation convention is used, and i, j = 1,2,3. T_{ij} is the dynamic Smagorinsky stress tensor which is similar to the τ_{ij} used in the constant Smagorinsky SGS model. For considering the interaction between the air and the particles, the following source term $\widetilde{\overline{S_{\mathrm{p},i}}}$ is implemented, cf. Eq. (6), with [41]

$$\widetilde{\overline{S_{\mathrm{p},i}}} = \sum_{i=1}^{n}\left[\frac{m_{\mathrm{p},i}}{\Delta V}\frac{(U_{\mathrm{p},i})_{t_{\mathrm{out}}} - (U_{\mathrm{p},i})_{t_{\mathrm{in}}}}{t_{\mathrm{out}} - t_{\mathrm{in}}}\right] \tag{7}$$

Through the Germano identity [40], the sub-grid stress tensor is a function of the resolved turbulent stress. Finally, using the viscosity hypothesis the sub-grid stress tensor [40], yields

$$T_{ij} - \left(\frac{\delta_{ij}}{3}\right)T_{kk} \approx -2\tilde{\bar{\Delta}}^2 \left|\tilde{\bar{S}}\right| \widetilde{\overline{S_{ij}}} \tag{8}$$

By substituting Eq. (2) and Eq. (7) in the Germano identity and multiplication by $\overline{S_{ij}}$ and finally averaging the equation, C_{s} is derived as

$$C_{\mathrm{s}} = -0.5\,\frac{\langle L_{kl}\bar{S}_{kl}\rangle}{\tilde{\bar{\Delta}}^2\langle \left|\tilde{\bar{S}}\right| \widetilde{\overline{S_{mn}}}\;\overline{S_{ij}}\rangle - \bar{\Delta}^2\langle \left|\tilde{\bar{S}}\right| \widetilde{\overline{S_{pq}}}\;\overline{S_{pq}}\rangle} \tag{9}$$

For obtaining the position, $\boldsymbol{x}_{\mathrm{p}}$, and velocity of the particles $\boldsymbol{U}_{\mathrm{p}}$, the Lagrangian particle tracking method is used as follows

$$\frac{d\boldsymbol{x}_{\mathrm{p}}}{dt} = \boldsymbol{U}_{\mathrm{p}} \tag{10}$$

$$\frac{d\boldsymbol{U}_{\mathrm{p}}}{dt} = \boldsymbol{F}_{\mathrm{D}} + \boldsymbol{g} = \frac{18\mu}{\rho_{\mathrm{p}} {d_{\mathrm{p}}}^2 C_{\mathrm{slip}}}\frac{C_{\mathrm{D}}\mathrm{Re}_{\mathrm{p}}}{24}\left(\widetilde{\overline{\boldsymbol{U}}} - \boldsymbol{U}_{\mathrm{p}}\right) + \boldsymbol{g} \tag{11}$$

In Eq. (11) $\boldsymbol{F}_{\mathrm{D}}$ and $\boldsymbol{g}$ are drag and gravitational acceleration, respectively. The drag coefficient can be obtained as follow [43]

$$C_{\mathrm{D}} = \begin{cases} \dfrac{24}{\mathrm{Re}_{\mathrm{p}}} & \text{if } \mathrm{Re}_{\mathrm{p}} \le 1000 \\ \dfrac{24}{\mathrm{Re}_{\mathrm{p}}}\left(1 + 0.15\,{\mathrm{Re}_{\mathrm{p}}}^{0.678}\right) & \text{if } \mathrm{Re}_{\mathrm{p}} \le 1000 \end{cases} \tag{12}$$

where, μ, Re_{p}, and ρ_{p} are the dynamic viscosity of the gas phase, the Reynolds number of the particle, and the particle density, respectively. C_{slip} is calculated as [44, 45]

$$C_{\mathrm{slip}} = 1 + \frac{2\lambda}{d_{\mathrm{p}}}\left[1.142 + 0.558\exp\left(-0.999\,\frac{d_{\mathrm{p}}}{2\lambda}\right)\right] \tag{13}$$

λ is the mean free path of the gas molecules which equals 0.0653 µm at the sea level and at room temperature [44].

2.2. Numerical Methods

The PISO method combined with SIMPLE solver (pimpleFoam solver) is implemented for numerical simulation [46-50] with OpenFOAM. The pimpleFoam solver is suitable for LES simulations with the dynamic Smagorinsky SGS model [51]. The dynamic Smagorinsky SGS model is used since it covers the laminar and the transitional turbulent-turbulent region so that it is very suitable for the simulation of the present flow which is predominantly laminar with possible transitional and turbulent flow regimes. In the dynamic Smagorinsky SGS model, C_s is dynamically chosen depending on the time and space. In order to model the particle phase, Lagrangian particle tracking is used which identifies the location of the particles by solving an ordinary differential equation [52]. The LagrangianParcel library in OpenFOAM is used to define the particle characteristics. Furthermore, the properties of water are used for the particles, because most of the drugs are aqueous solutions so that their densities are very close to that of water [53]. The simulations are run for a real time of one second. This time is chosen, since after 1 s more than 99% of the particles are deposited on the wall or are escaped from the nasal cavity into the pharynx. The computer cluster "bwForCluster MLS & WISO" is used to perform the simulations with 256 CPUs and a constant time step of 10^{-5} s. Based on Figure 4, the nasal cavity was divided into three main parts: the wall, inlet and outlet. The nosepieces are extended to represent the fully developed condition [18, 54]. Second order central differencing discretization schemes are used. The Dirichlet boundary condition is used for the inlet velocity which follows a sinusoidal velocity profile, cf. Fig. 6. The gas velocity at the inlet is equal to 0.94 m/s which corresponds to the airflow rate generated by PARI SINUS compressor at an inflow rate of 4.78 L/min. The following equation describes the velocity profile at the inlet

$$U = U_0 + U_0 \sin(2\pi\omega t), \tag{14}$$

where ω is 45 Hz as prescribed by PARI SINUS. Thus, the pulsating gas velocity profile displayed in Fig. 6 is considered for the inlet boundary condition.

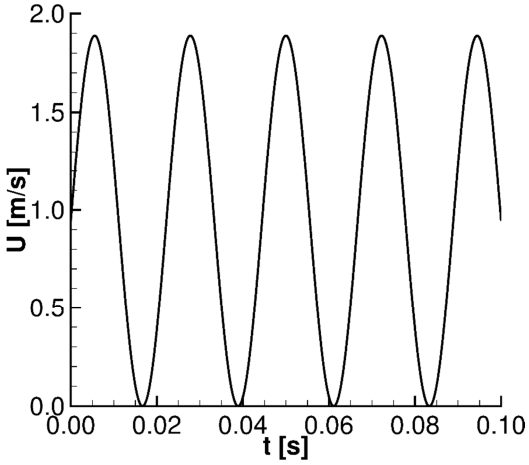

Figure 6. Pulsating velocity that is considered for the inlet B.C.

10,000 particles are uniformly and randomly injected at one nostril and the experimental particle size distribution is implemented that was provided by PARI GmbH for the PARI SINUS nebulizer. The MMD and the Sauter mean diameter were reported as 3.33 µm and 2.4 µm, respectively. Furthermore, the geometric standard deviation (GSD) was 1.93 µm.

3. Results and Discussion

For validating the numerical simulation, the same geometry and boundary conditions of the experimental study of Pui et al. [55] are generated and a particle-laden flow simulation is performed. The particles and the airflow with Reynolds number of 1,000 enter the computational domain through the horizontal pipe and they exit from the vertical pipe with diameter 5.03 mm. Different simulations for mono-disperse particles with size 1-50 µm are performed. Ten thousand particles are randomly and uniformly injected at the inlet. The curvature ratio of 5.7 is used for the pipe to match the conditions of the experiments. Furthermore, the properties of uranine are considered for the particle phase as used in experiments of Pui et al. [55]. Figure 7 shows the geometry of the 90° bend pipe and its mesh at the inlet plane.

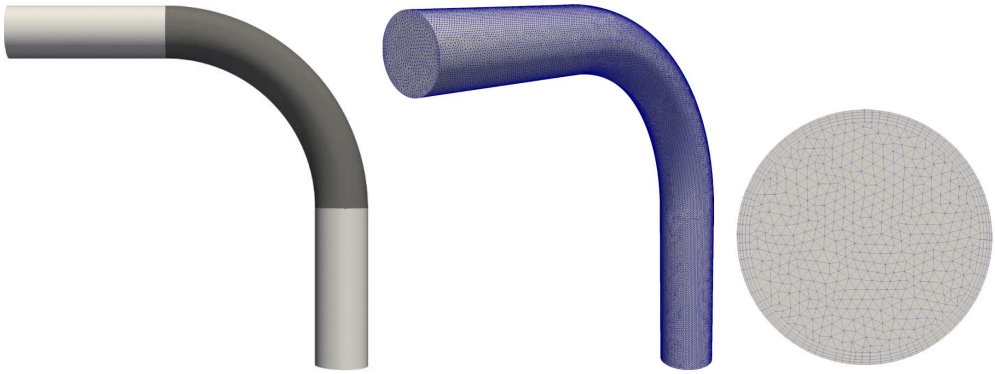

Figure 7. The geometry of the 90° bend pip (left), surface mesh of the 90° bend pipe (center), and surface mesh of the inlet cross section (right).

With the definition of the Stokes number

$$\mathrm{St} = \frac{C_{\mathrm{slip}}\rho_{\mathrm{p}}d_{\mathrm{p}}\boldsymbol{U}_0^2}{18\mu a_{\mathrm{t}}} \tag{15}$$

where C_{slip}, ρ_{p}, d_{p}, $\mathbf{U}_0$, μ, a_t are the Cunningham slip correction fraction, the density of the particle, the particle diameter, the mean gas axial velocity in the bend, the dynamic viscosity of the fluid and the radius of the tube, respectively [55], the DE versus Stokes number is shown in Fig. 8. The results show a good agreement between the numerical simulations and the experimental data. Figure 8 shows that the present results lie well within the regime of other results which validates the present model.

The pressure drop in the nasal cavity versus the inlet flow rate is shown in Fig. 9 [56, 57]. The results of the current simulations with two different inlet airflow rates of 4.78 L/min and 7.5 L/min are compared with the experimental and numerical studies available in the literature [56-60]. There are slight differences in the results which are due to the differences in the patient-specific geometry of these models. Furthermore, the experimental results are affected by the undesirable roughness in the surface of the nasal cavity during the construction procedure. In the present simulations, the values of pressure drop for inlet flow rates of 4.75 L/min and 7.5 L/min are 5 Pa and 9 Pa, respectively. Although the geometries of the nasal cavities are different, the present pressure drop in the cavity is in good agreement with those of Schroeter et al. [57], model C, where the surface smoothness was enhanced to obtain a more realistic anatomical geometry. In model A [57], they applied no surface smoothness to preserve all attributes of the replica cast used by Kelly et al. [56] which leads to higher pressure drop for a specific flow rate. The differences in the results with other models shown in Fig. 9 is due to the individual variability of the human nasal cavities.

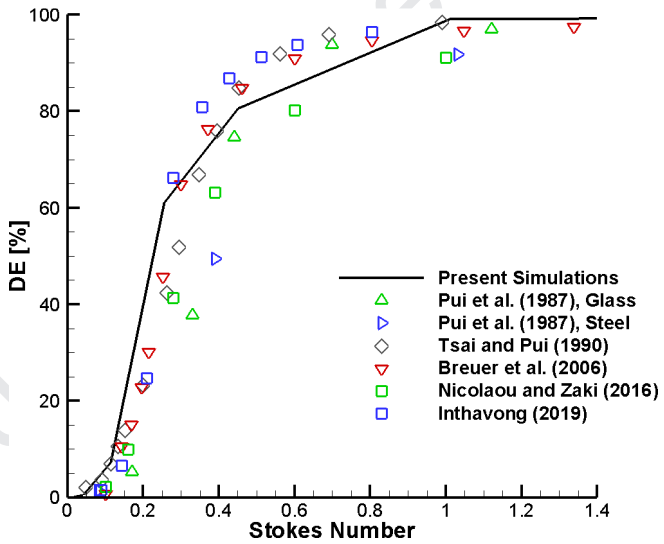

Figure 8. Comparison between the present numerical solutions for a 90° bend and the experimental and numerical deposition efficiency data on the same geometry available in the literature for the experimental setup of Pui et al. [55] with Re = 1,000 [55, 61-64].

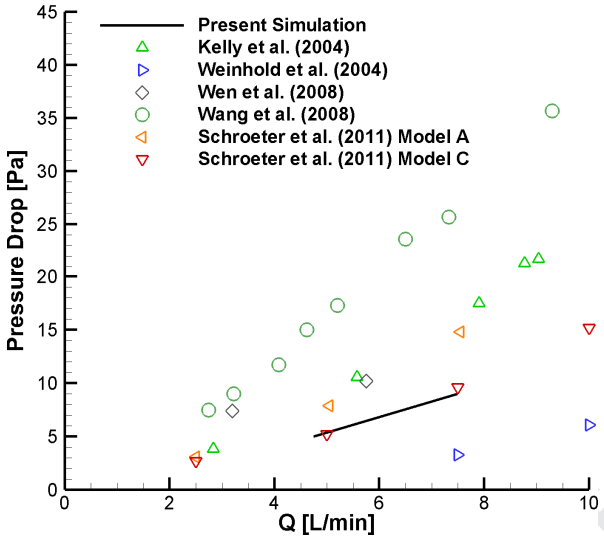

Figure 9. Comparison of the pressure drop versus the inlet airflow rate with the experimental and numerical data available in the literature [56-60]. The effects of flow rates and patient-specific geometries on pressure drop (open soft palate condition) [36].

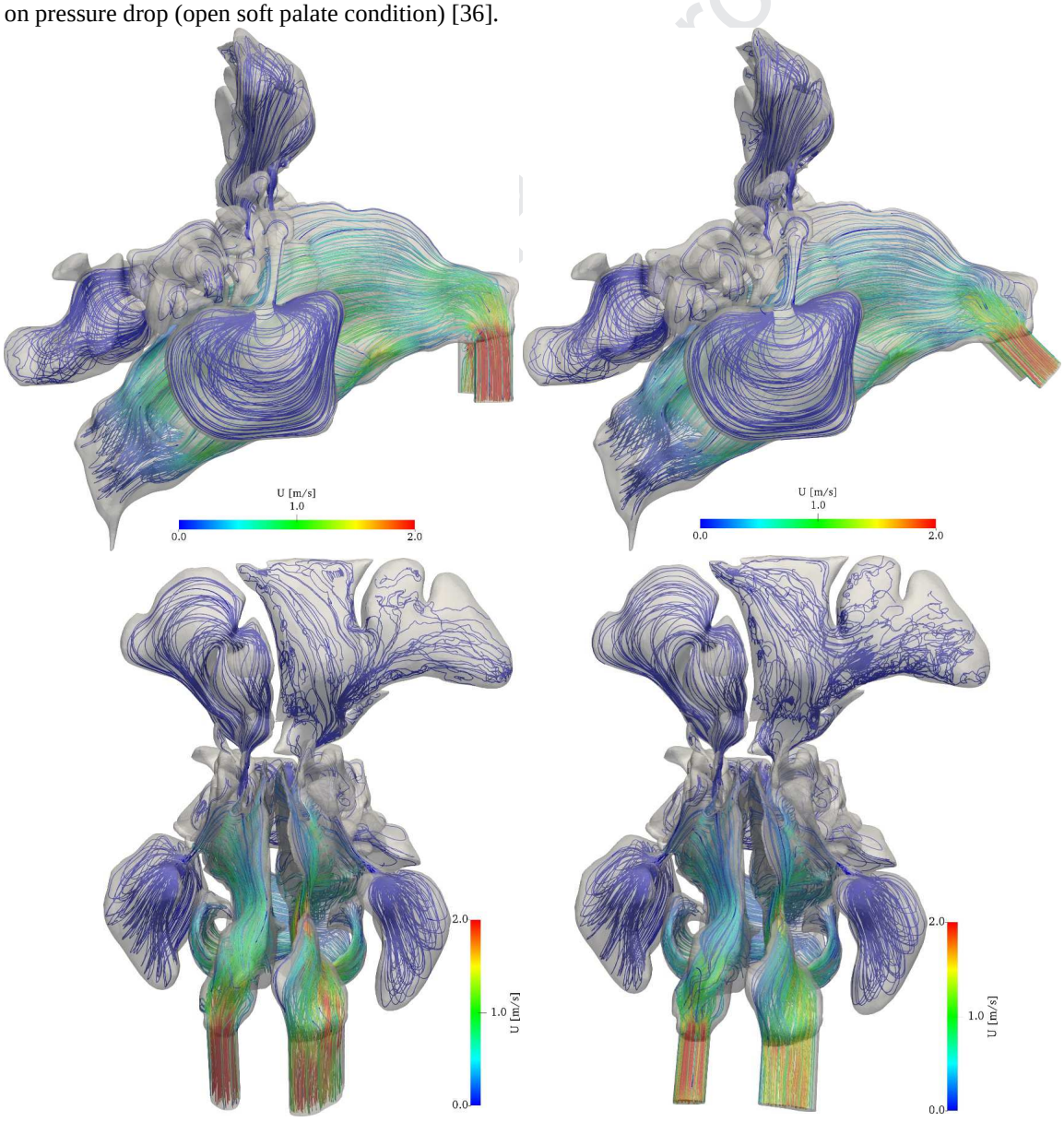

Figure 10. Streamlines of the pulsating airflow inside the realistic nasal cavity with 90° (left) and 45° (right) nosepieces at t = 0.02775 s.

Figure 10 shows the streamlines of the air velocity in the nasal cavity with 90° and 45° nosepieces at the maximum peak of the inlet velocity profile corresponding to t = 0.02775 s. In contrast to the constant inlet velocity condition which causes recirculation zones after the nasal valve due to the sudden expansion of the airway geometry [36], the pulsating inlet airflow avoids recirculation zones after the nasal valve. At t = 0.03885 s, the inlet velocity is zero and the streamlines of the gas velocity show a very complex pattern in the nasal airway including recirculation zones and swirling flow in different regions of the cavity, see Fig. 11.

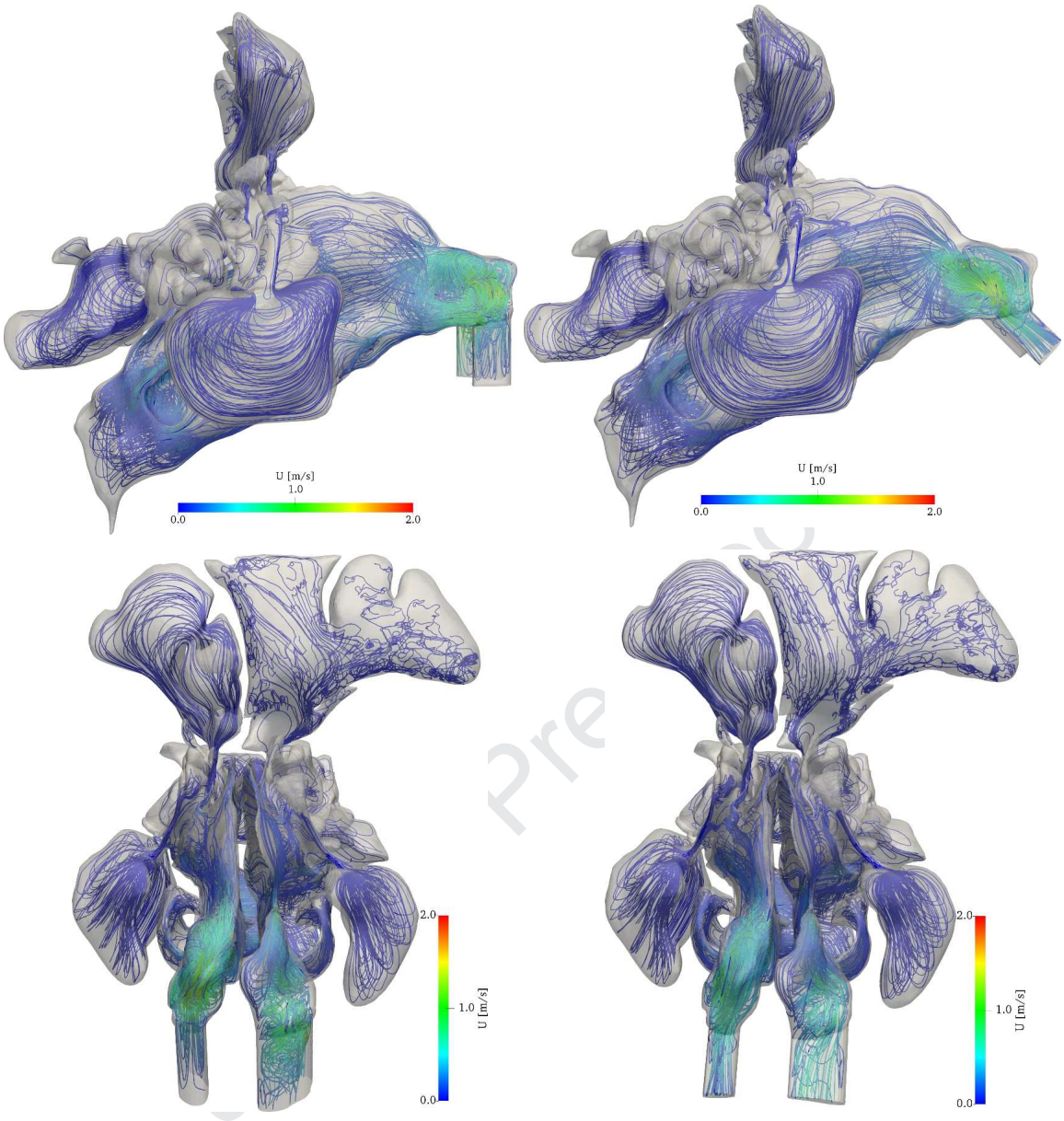

Figure 11. Streamlines of the pulsating airflow inside the realistic nasal cavity with 90° (left) and 45° (right) nosepieces at t = 0.03885 s.

In order to study the amount of the airflow reaching each sinus, the concentration of a scalar tracer is calculated in the computational domain which shows the amount of air entering from inlet in each region. The value of C lies between zero and unity, where unity in a specific region shows that the air from the inlet has reached that specific region. For C equals zero in a region, there is no air ventilation in that specific region. A detailed analysis of the variable C is performed in the right and the left maxillary and the frontal and sphenoid sinuses.

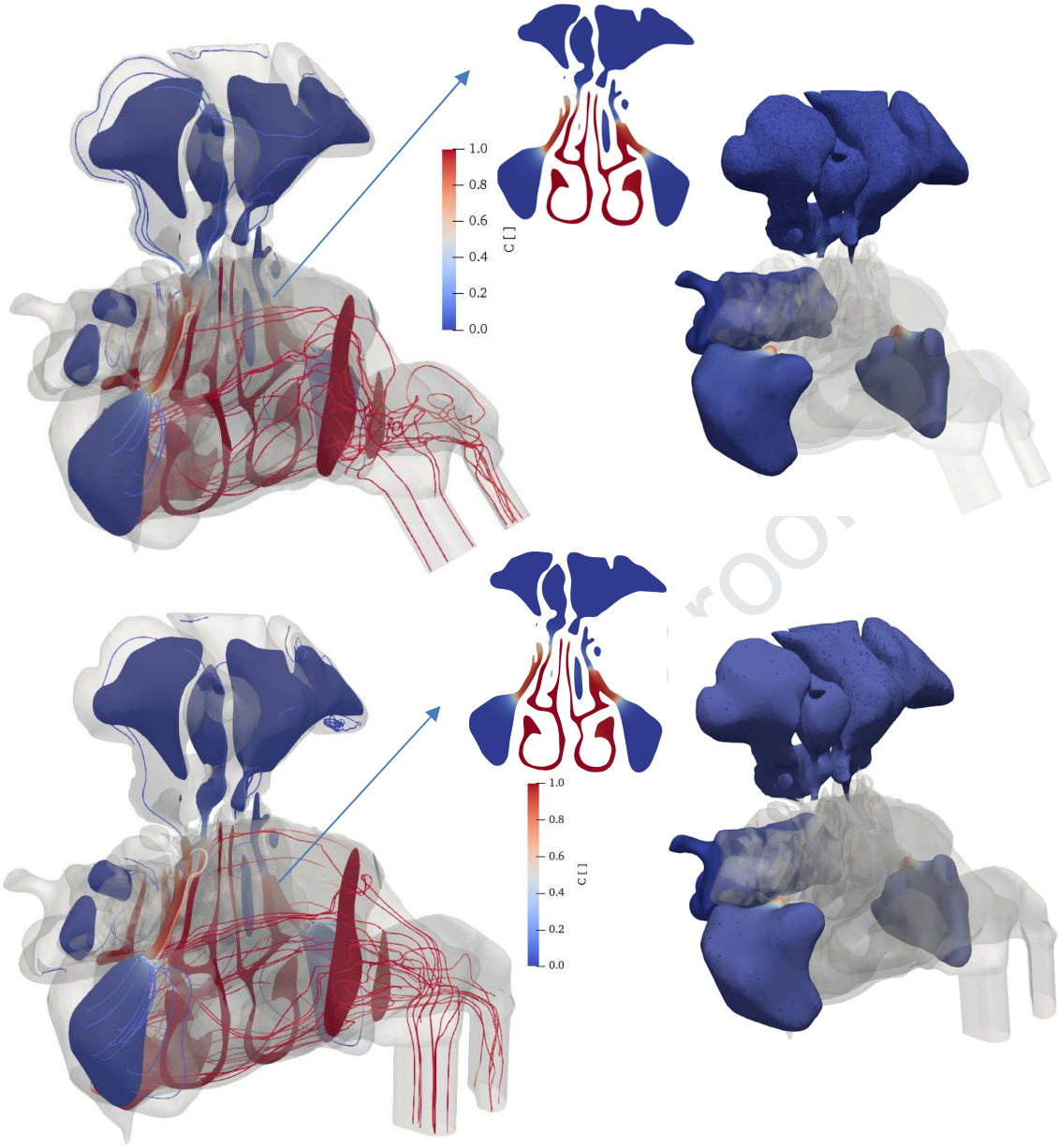

Figure 12. The contour plots and streamlines of variable C for 45° (top) and 90° nosepieces (bottom) nosepieces at t = 1 s.

The air from the inlet reaches to the entrance of the paranasal sinuses, however, it does not completely enter the sinuses, and the values of C at the sinuses are very low which reflect the low air ventilation inside the sinuses with both 90° and 45° nosepieces after 1 s of real time simulations, see Fig. 12. The flow partitions inside each sinus are quantified by dividing the integral of the variable C in the volume of each sinus by the integral of C in the whole nasal domain, and quantitative results are presented in Fig. 13. The quantitative analysis shows that utilization of 45° nosepiece leads to a slight improvement of the ventilation of the right and left

maxillary and the sphenoid sinuses. In the right and left frontal sinuses, the air ventilation is approximately equal for 45° and 90° nosepieces. When the inlet pipe is inserted into the right nostril (as done in this study), there is a remarkable improvement in the ventilation of right maxillary and frontal sinuses compared to left maxillary and frontal sinuses for both 90° and 45° nosepieces. However, the flow fractions in the left sphenoid sinuses are higher than in the right sphenoid sinuses in both 45° and 90° nosepieces.

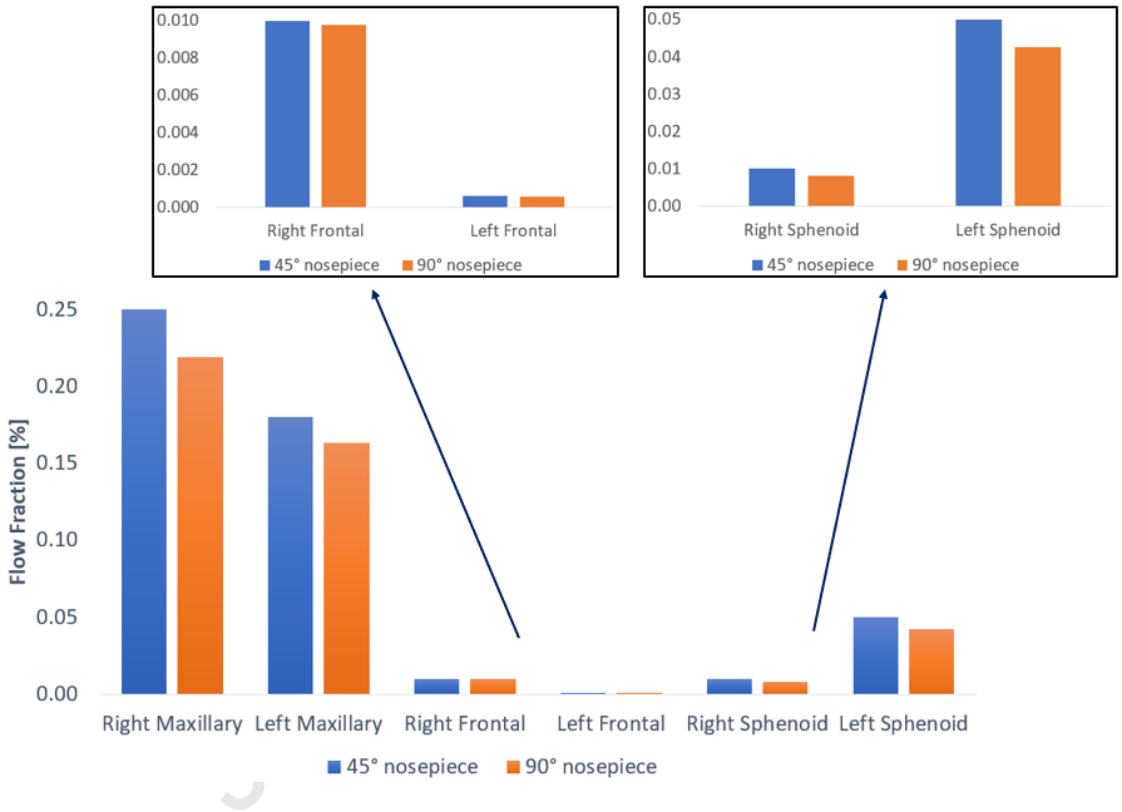

Figure 13. The flow fraction in right and left maxillary, sphenoid, and frontal sinuses with 45° and 90° nosepieces.

Figure 14 displays the evolution of the particles carried by the pulsating airflow entered through a 90° nosepiece. At t = 0.00555 s, the inlet velocity is at the maximum value of the first pulse and the particles are still in the 90° nosepiece. At t = 0.0222 s, the first pulse ends and the particles reach the vestibule and nasal valve and some parts are still inside the 90° nosepiece. At t = 0.0555 s which corresponds to the peak of the third pulse, the particles enter the main nasal passage and some are in the nasal valve and a small portion already deposited in the vestibule. At the end of the fifteenth pulse at t = 0.333 s, some of the particles have reached the other nostril and exited the computational domain. Some particles are still floating inside the nasal cavity and some have deposited on the inner surface of the nasal cavity. The evolution of the

particles depicts the general path of the particles in the nasal passage. The particles move through the right nasal passage and experience a 180° change in the airflow direction in the nasopharynx. Afterward, the particles pass through the other side of the cavity and finally exit the nasal airway through the other nostril. The pulsating airflow supports the particles to pass through the olfactory region since there is no recirculation zone after the nasal valve at the expansion of the cavity which occurs in the drug delivery with constant flow rate at the inlet.

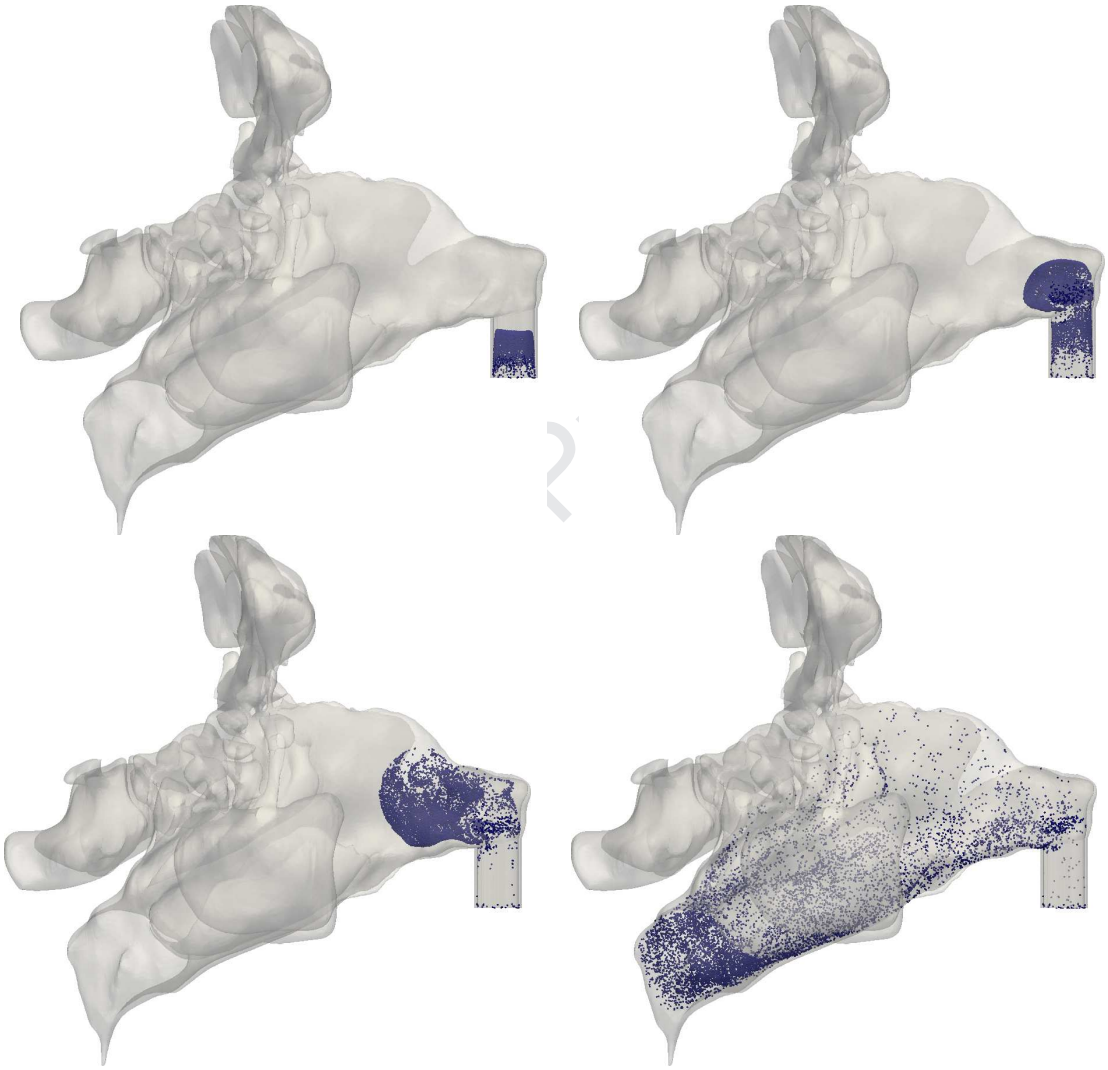

Figure 14. Time marching of the poly-disperse particles (MMD =3.33 µm, GSD = 1.93 µm) carried by a pulsating airflow entered through a 90° nosepiece at t = 0.00555 s, t = 0.0222 s, t = 0.0555 s and t = 0.333 s (from top-left to bottom-right).

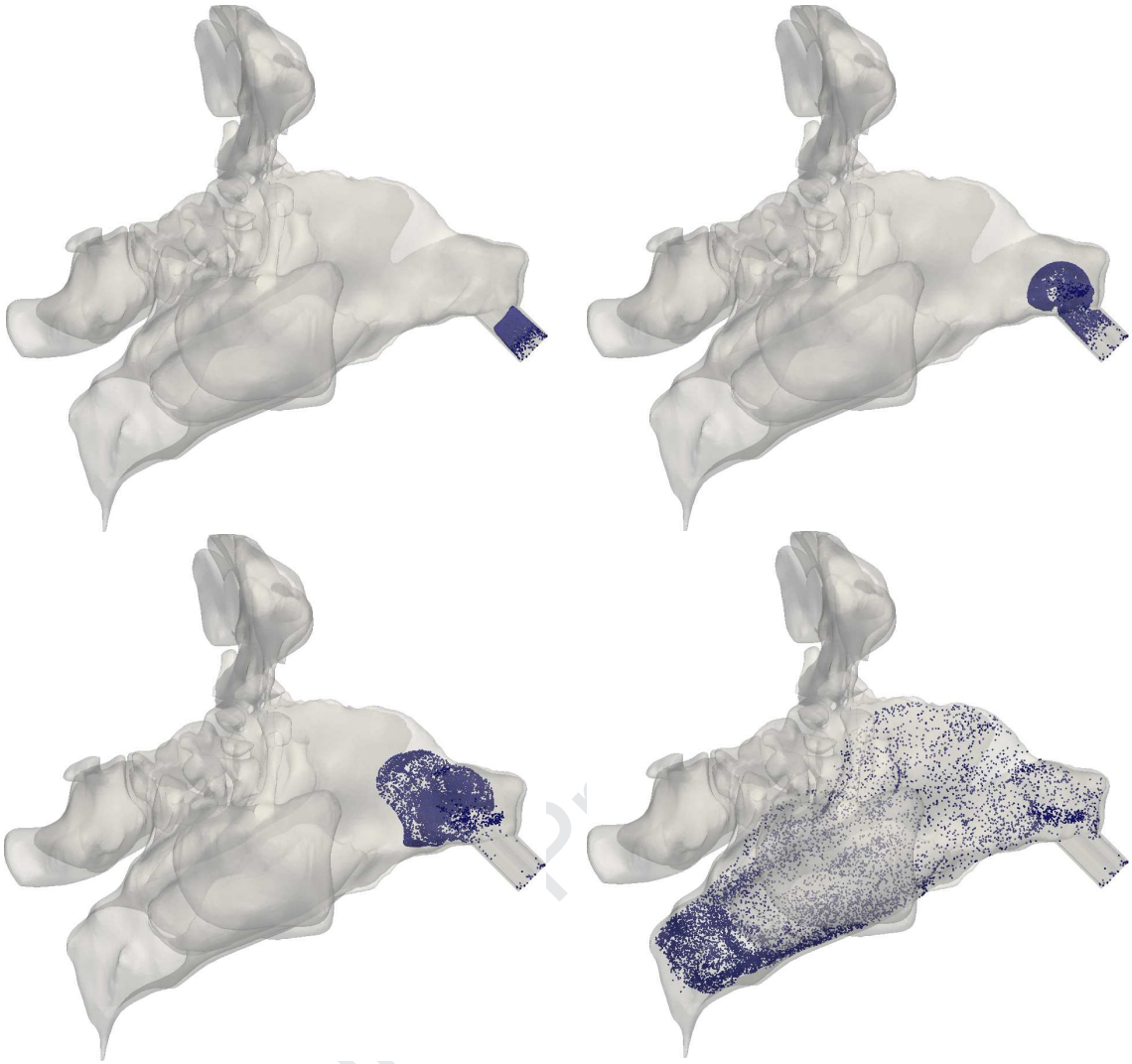

Figure 15. Temporal evolution of the poly-disperse particles (MMD =3.33 µm, GSD = 1.93 µm) carried by a pulsating airflow entered through a 45° nosepiece at t = 0.00555 s, t = 0.0222 s, t = 0.0555 s and t = 0.333 s (from top-left to bottom-right).

Similarly, Fig. 15 shows the evolution of the particles during pulsating, bi-directional drug delivery with a 45° nosepiece. At t = 0.00555 s, the velocity at the inlet plane is at the peak of the first pulse, the particles reside inside the 45° nosepiece. At t = 0.0222 s, the inlet velocity is at the end of the first pulse, particles enter the nasal valve and some particles still reside inside the nosepiece. At t = 0.0555 s, some particles enter the main nasal passage whereas others still reside in the nasal valve region. At the nasal valve, an air jet is created due to reduction of the cross-sectional area of the cavity which causes the enhancement of the gas velocity and consequently increasing the velocity of the particles. At t = 0.333 s, some particles still reside inside the right cavity and some particles have reached the left nasal cavity and even exited through the other nostril. Since the nasopharynx and pharynx are disconnected, the airflow carries the particles from one cavity to the other cavity. The evolution of the particles during the nasal drug delivery processes with 90° and 45° nosepieces show that the 45° nosepiece

improves the deposition pattern of the particles at the upper parts of the cavity especially at the downstream of the nasal valve, see Figs. 14 and 15.

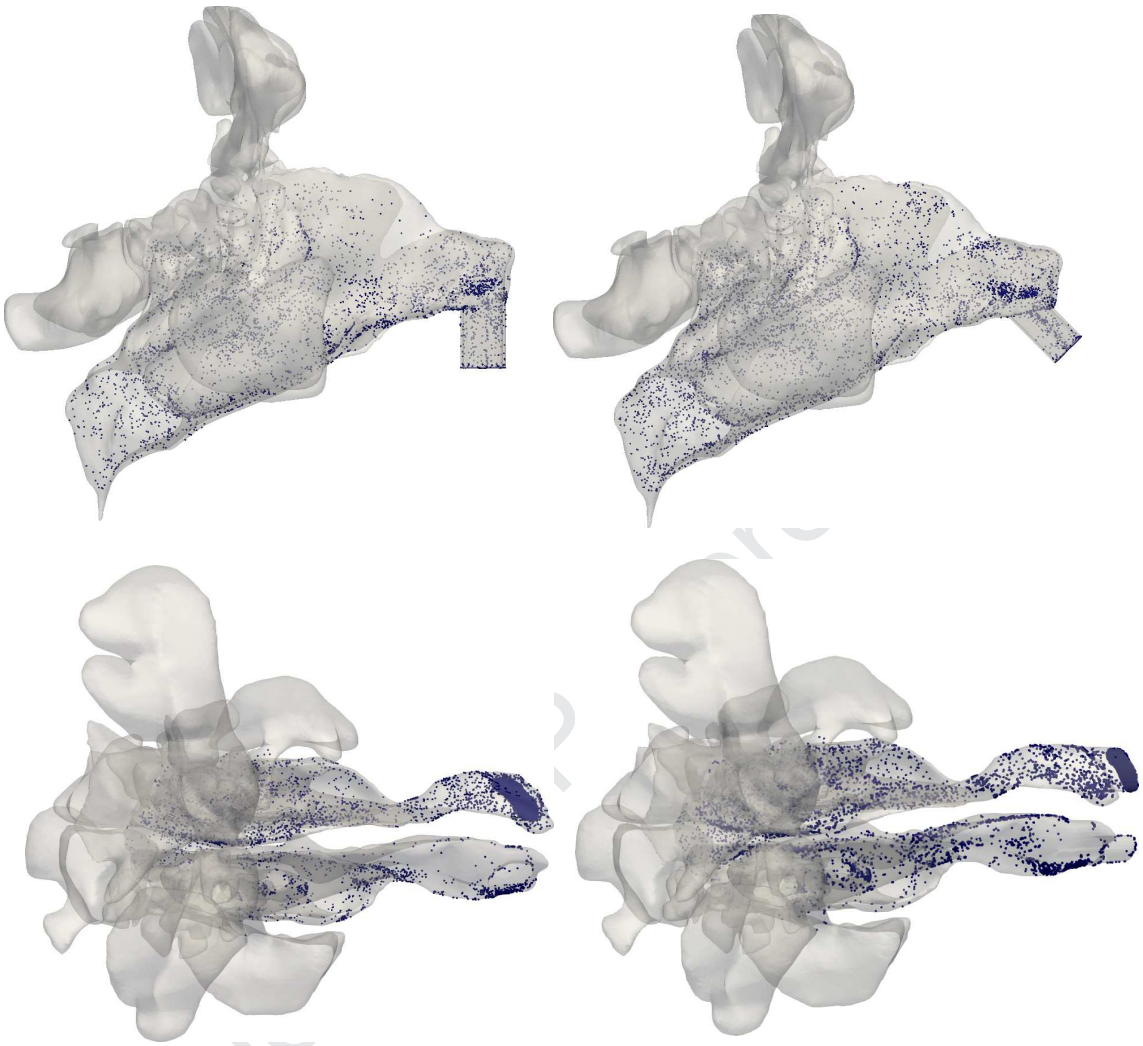

Figure 16. Particle deposition pattern after 1 s of bi-directional pulsating drug delivery using 90° (left) and 45° (right). Particles enter through the right nostril and exit the domain from the left nostril.

Figure 16 shows the deposition pattern of the particles using 90° and 45° nosepieces at t = 1 s which is the end of the simulation. The effects of the angle of the nosepieces on the deposition pattern of the particles are illustrated. The results depict that in both cases, deposition of the particles in the nasal valve and middle turbinates are slightly higher than in the other regions of the nasal cavity. However, the deposition pattern of the particles in the whole nasal cavity is relatively uniform. The main difference in the deposition pattern is observed behind the nasal valve, where the deposition at the upper parts of the nasal cavity and turbinates is enhanced with the 45° nosepiece. The utilization of 90° and 45° nosepieces result in total DEs of 41.5 % and 48.7 %, respectively, compared to the non-pulsating airflow, which is an improvement of the DE by approximately 17 % for the 45° nosepiece compared to the 90° nosepiece. Möller et al.

[11] reported a DE of 58 ± 17 % for the bi-directional pulsating aerosol delivery with PARI SINUS in healthy volunteers. For the same device of PARI SINUS with inlet airflow rate of 6 L/min, the in vitro study of Xi et al. [31] give a DE of 24 ± 6 %. Furthermore, the very low deposition rate of particles inside sinuses are in agreement with the in-vitro study of Xi et al. [31].

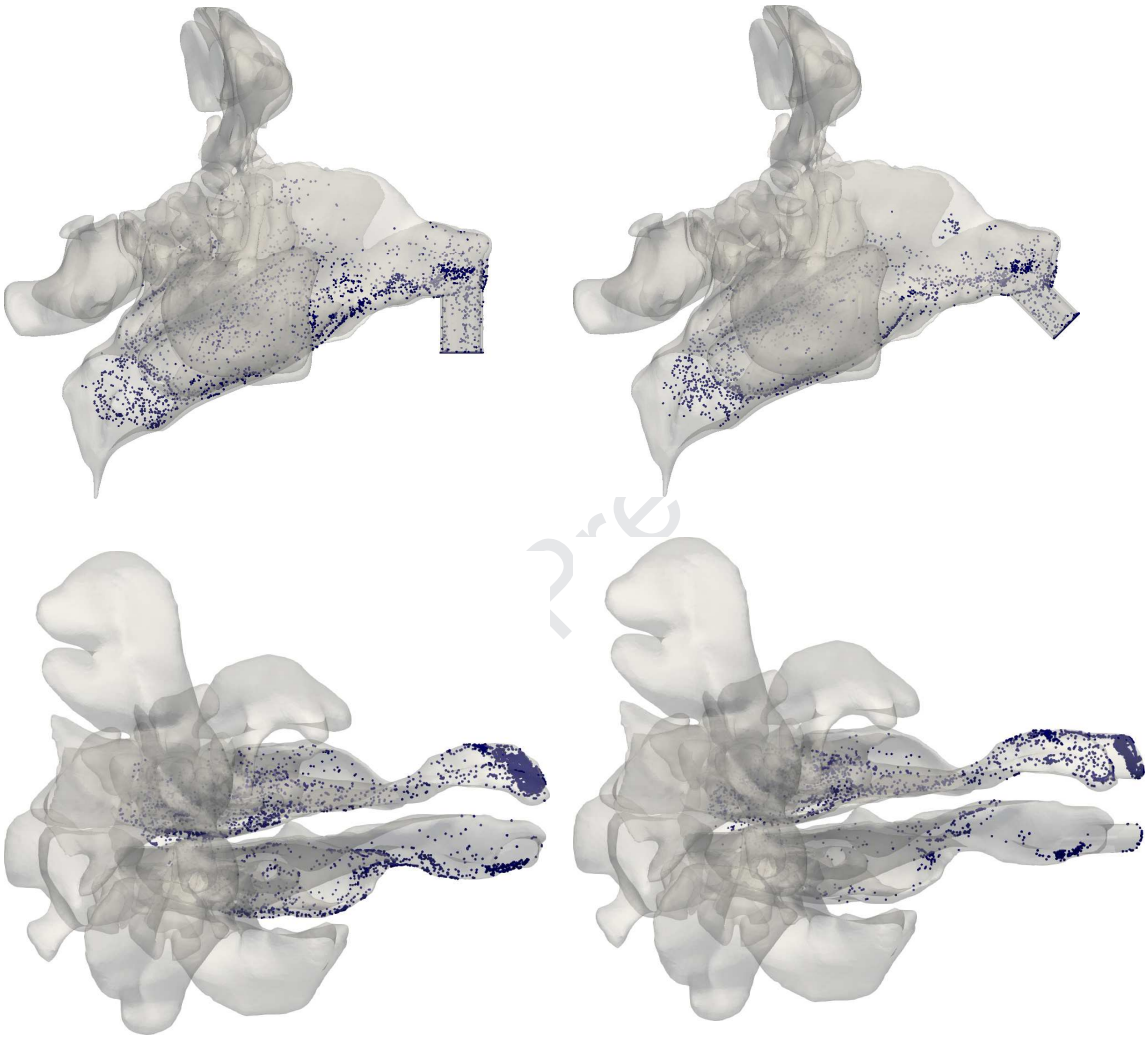

Figure 17. Particle deposition pattern after 1 s of bi-directional drug delivery with constant (non-pulsating) inlet airflow of 4.78 L/min using 90° (left) and 45° (right) nosepices. Particles enter the cavity through right nostril and exit the airway from the left nostril.

These DEs of pulsating aerosol delivery may be compared to non-pulsating DEs. Figure 17 depicts the deposition pattern of the particles carried by a constant (non-pulsating) flow rate of 4.78 L/min which corresponds to the average value of the pulsating airflow in this study using both the clockwise 90° and 45° nosepieces. In this situation, particles mainly deposit in the lower parts of the cavity and at the nasal valve. After the nasal valve where the geometry expands, particles are not moving to the upper parts of the nasal cavity for a constant inlet flow which is greatly improved for the pulsating airflow as seen in comparing Figs. 16 and 17. Due

to the sharper bend in the case of 90° nosepiece, more particles deposit in the nasal cavity compared to the 45° nosepiece. The simulations of the non-pulsating inlet airflow result in DEs of 28.7 % and 18.7 % for the nosepieces with 90° and 45° bending, respectively. It is remarkable that for the steady inflow, the use of the 90° nosepiece shows a higher total DE than the 45° nosepiece, reversing the results of the pulsating airflow. For the steady inflow, the use of the 90° nosepiece causes the flow to impinge and particles deposit directly to the wall of the nasal valve (outer wall of the 90° curve), however, using the 45° nose piece, the particle impingement to the outer wall of the 90°curve at the nasal valve is reduced. For the pulsating condition, there is no strong impingement as in the steady inflow since the oscillation of the flow damps the impingement of the particles at the nasal valve that was observed in the case of the steady airflow. This eventually leads to higher DE for the 90° nosepiece for the steady inflow and a lower DE for the pulsating airflow. DEs for bi-directional non-pulsating and pulsating aerosol delivery with clockwise 45° nosepiece are18.7 % and 48.7 %, respectively, which show approximately 160 % enhancement in DE when the pulsating airflow is used. Moreover, DEs for bi-directional non-pulsating and pulsating aerosol delivery with 90° nosepiece result in 28.7 % and 41.5 % depicting a 44.6 % increase in DE with utilization of pulsating inflow rates. The pulsating and non-pulsating results are comparable to the in-vivo data of Möller et al. [11] who reported DEs of 58 ± 17 % and 25 ± 16 %, respectively, for drug delivery in three healthy human volunteers with pulsating and non-pulsating airflow of the PARI SINUS device. The differences in the results originate from the specific differences in the nasal anatomies [23, 26], different MMD of the particles and different inlet flow rates.

Moreover, the deposition pattern of the particles carried by a pulsating airflow driven from both nostrils (open soft palate condition) for the same geometry without resolving the paranasal sinuses and using a 90° nosepiece lead to a DE of less than 8 % [36]. The utilization of bi-directional drug delivery (closed soft palate condition) results in DEs of 41.5 % which shows a remarkable enhancement of the DE by more than fourfold in comparison to the open soft palate condition where both the airflow and the particles enter from both nostrils and exit through the nasopharynx.

4. Conclusions

In the present study, a workflow has been developed to predict personalized human nasal drug delivery efficiency for pulsating bi-directional aerosol delivery (here: PARI SINUS). The patient keeps the mouth open and pushes his tongue towards the soft palate to create the closed soft palate condition which enables the bi-directional drug delivery. The three-dimensional geometric of the nasal cavity, which is reconstructed from CT images of a specific patient, is used to perform numerical simulations of the inhaled airflow and associated particle deposition.

Calculations are performed for two different nosepiece angles and the results are compared. Results show that the utilization of the drug delivery device with a clockwise inclination of 45° with respect to the horizontal axis results in a more efficient drug delivery in comparison to the clockwise 90° nosepiece. For the present situation where the drug delivery is initiated from the right nostril, the air ventilation in the right maxillary and in frontal sinuses is remarkably higher than in the left maxillary and the frontal sinuses with both 45° and 90° nosepieces. In contrast, the flow fraction in the left sphenoid sinus is higher than the right sphenoid sinus. The utilization of the clockwise 45° nosepiece leads to slightly better ventilation than the usage of a clockwise 90° nosepiece in all paranasal sinuses except frontal sinuses where approximately equal flow fraction is observed. The flow partition analysis show improvement in ventilation of the right maxillary sinus from 0.22% to 0.25%. Pulsating bi-directional drug delivery enhances the DE and leads to a more uniform deposition pattern of the particles inside the nasal airway. Therefore, the utilization of bi-directional drug delivery with a clockwise 45° nosepiece and a pulsating airflow is recommended.

5. Acknowledgements

The authors thank Dr. H. Mentzel from PARI Respiratory Equipment Inc. for providing the particle size distribution profile. Furthermore, the high-performance computing time at the bwForCluster MLS & WISO Production is acknowledged which is funded by the state of Baden- Württemberg through bwHPC and German Research Foundation (DFG) through grant INST 35/1134-1 FUGG. Ali Farnoud acknowledges financial support of the DFG through HGS MathComp.

6. References

[1] K.I. J. Tu, and G. Ahmadi, Computational Fluid and Particle Dynamics in the Human Respiratory System, Springer2013.
[2] J.D. Suman, Current understanding of nasal morphology and physiology as a drug delivery target, Drug Deliv Transl Res, 3 (2013) 4-15.
[3] J.D. Suman, B.L. Laube, R. Dalby, Comparison of nasal deposition and clearance of aerosol generated by a nebulizer and an aqueous spray pump, Pharmaceutical Research, (1999).
[4] W. Möller, U. Schuschnig, G. Celik, W. Münzing, P. Bartenstein, K. Häussinger, W.G. Kreyling, M. Knoch, M. Canis, S. Becker, Topical drug delivery in chronic rhinosinusitis patients before and after sinus surgery using pulsating aerosols, PloS one, 8 (2013) e74991-e74991.
[5] C. Hilton, T. Wiedmann, D. Ph, M.S. Martin, B. Humphrey, R. Schleiffarth, F. Rimell, Differential deposition of aerosols in the maxillary sinus of human cadavers by particle size, (2017) 395-398.

[6] S.K. Kim, S.K. Chung, An investigation on airflow in disordered nasal cavity and its corrected models by tomographic PIV, Measurement Science and Technology, 15 (2004) 1090-1096.
[7] D. Doorly, D.J. Taylor, P. Franke, R.C. Schroter, Experimental investigation of nasal airflow, Proceedings of the Institution of Mechanical Engineers, Part H: Journal of Engineering in Medicine, (2008).
[8] S. Hosseini, L. Golshahi, An in vitro evaluation of importance of airway anatomy in sub-regional nasal and paranasal drug delivery with nebulizers using three different anatomical nasal airway replicas of 2-, 5- and 50-Year old human subjects, International journal of pharmaceutics, 563 (2019) 426-436.
[9] M. Durand, S. Le Guellec, J. Pourchez, F. Dubois, G. Aubert, G. Chantrel, L. Vecellio, C. Hupin, R. De Gersem, G. Reychler, L. Pitance, P. Diot, F. Jamar, Sonic aerosol therapy to target maxillary sinuses, European Annals of Otorhinolaryngology, Head and Neck Diseases, 129 (2012) 244-250.
[10] D. Elad, R. Liebenthal, B.L. Wenig, S. Einav, Analysis of Air-Flow Patterns in the Human Nose, Medical & Biological Engineering & Computing, 31 (1993) 585-592.
[11] W. Möller, U. Schuschnig, G. Meyer, K. Häussinger, M. Keller, B. Junge-Hülsing, H. Mentzel, Ventilation and aerosolized drug delivery to the paranasal sinuses using pulsating airflow a preliminary study, Rhinology, 47 (2009) 405-412.
[12] W. Möller, U. Schuschnig, G. Khadem Saba, G. Meyer, B. Junge-Hülsing, M. Keller, K. Häussinger, Pulsating aerosols for drug delivery to the sinuses in healthy volunteers, Otolaryngology - Head and Neck Surgery, 142 (2010) 382-388.
[13] K. Keyhani, P.W. Scherer, M.M. Mozell, Numerical Simulation of Airflow in the Human Nasal Cavity, Journal of Biomechanical Engineering, 117 (1995) 429-441.
[14] R.P. Subramaniam, R.B. Richardson, K.T. Morgan, J.S. Kimbell, R.A. Guilmette, Computational Fluid Dynamics Simulations of Inspiratory Airflow in the Human Nose and Nasopharynx, Inhalation Toxicology, 10 (1998) 91-120.
[15] K. Inthavong, Z.F. Tian, H.F. Li, J.Y. Tu, W. Yang, C.L. Xue, C.G. Li, A Numerical Study of Spray Particle Deposition in a Human Nasal Cavity, Aerosol Science and Technology, 40 (2006) 1034-1045.
[16] K.T. Shanley, P. Zamankhan, G. Ahmadi, P.K. Hopke, Y.-S. Cheng, Numerical simulations investigating the regional and overall deposition efficiency of the human nasal cavity, Inhalation toxicology, 20 (2008) 1093-1100.
[17] A. Farnoud, X. Cui, I. Baumann, E. Gutheil, Numerical analysis of the flow and particles pattern in the human nasal cavity, ICMF 2016Firenze, 2016.
[18] H. Shi, C. Kleinstreuer, Z. Zhang, Modeling of inertial particle transport and deposition in human nasal cavities with wall roughness, Journal of Aerosol Science, 38 (2007) 398-419.
[19] H. Shi, C. Kleinstreuer, Z. Zhang, Laminar Airflow and Nanoparticle or Vapor Deposition in a Human Nasal Cavity Model, Journal of Biomechanical Engineering, 128 (2006) 697-706.
[20] H. Shi, C. Kleinstreuer, Simulation and Analysis of High-Speed Droplet Spray Dynamics, Journal of Fluids Engineering, 129 (2006) 621-633.
[21] V. Covello, C. Pipolo, A. Saibene, G. Felisati, M. Quadrio, Numerical simulation of thermal water delivery in the human nasal cavity, Computers in Biology and Medicine, 100 (2018) 62-73.
[22] H. Calmet, A.M. Gambaruto, A.J. Bates, M. Vázquez, G. Houzeaux, D.J. Doorly, Large-scale CFD simulations of the transitional and turbulent regime for the large human airways during rapid inhalation, Computers in Biology and Medicine, 69 (2016) 166-180.

[23] H. Calmet, C. Kleinstreuer, G. Houzeaux, A.V. Kolanjiyil, O. Lehmkuhl, E. Olivares, M. Vázquez, Subject-variability effects on micron particle deposition in human nasal cavities, Journal of Aerosol Science, 115 (2018) 12-28.
[24] P.G. Djupesland, A. Skretting, M. Winderen, T. Holand, Breath actuated device improves delivery to target sites beyond the nasal valve, Laryngoscope, (2006).
[25] P.G. Djupesland, A. Skretting, Nasal Deposition and Clearance in Man: Comparison of a Bidirectional Powder Device and a Traditional Liquid Spray Pump, Journal of Aerosol Medicine and Pulmonary Drug Delivery, (2012).
[26] M. Kleven, M.C. Melaaen, M. Reimers, J.S. Røtnes, L. Aurdal, P.G. Djupesland, Using Computational Fluid Dynamics (CFD) to Improve the Bi-Directional Nasal Drug Delivery Concept, Food and Bioproducts Processing, 83 (2005) 107-117.
[27] D.O. Frank, J.S. Kimbell, D. Cannon, J.S. Rhee, Computed intranasal spray penetration: Comparisons before and after nasal surgery, International Forum of Allergy and Rhinology, (2013).
[28] M. Durand, J. Pourchez, G. Aubert, S. Le Guellec, L. Navarro, V. Forest, P. Rusch, M. Cottier, Impact of acoustic airflow nebulization on intrasinus drug deposition of a human plastinated nasal cast: New insights into the mechanisms involved, International Journal of Pharmaceutics, 421 (2011) 63-71.
[29] W. Möller, U. Schuschnig, G. Meyer, H. Mentzel, M. Keller, Ventilation and drug delivery to the paranasal sinuses: Studies in a nasal cast using pulsating airflow, Rhinology, 46 (2008) 213-220.
[30] W. Moller, U. Schuschnig, P. Bartenstein, G. Meyer, K. Haussinger, O. Schmid, S. Becker, Drug delivery to paranasal sinuses using pulsating aerosols, J Aerosol Med Pulm Drug Deliv, 27 (2014) 255-263.
[31] J. Xi, X.A. Si, S. Peters, D. Nevorski, T. Wen, M. Lehman, Understanding the mechanisms underlying pulsating aerosol delivery to the maxillary sinus: In vitro tests and computational simulations, International Journal of Pharmaceutics, 520 (2017) 254-266.
[32] J. Xi, J.E. Yuan, X.A. Si, J. Hasbany, Numerical optimization of targeted delivery of charged nanoparticles to the ostiomeatal complex for treatment of rhinosinusitis, Int J Nanomedicine, 10 (2015) 4847-4861.
[33] J. Xi, Z. Wang, X.A. Si, Y. Zhou, Nasal dilation effects on olfactory deposition in unilateral and bi-directional deliveries: In vitro tests and numerical modeling, European Journal of Pharmaceutical Sciences, 118 (2018) 113-123.
[34] J. Xi, Z. Wang, D. Nevorski, T. White, Y. Zhou, Nasal and Olfactory Deposition with Normal and Bidirectional Intranasal Delivery Techniques: In Vitro Tests and Numerical Simulations, J Aerosol Med Pulm Drug Deliv, 30 (2017) 118-131.
[35] L. Leclerc, J. Pourchez, G. Aubert, S. Leguellec, L. Vecellio, M. Cottier, M. Durand, Impact of Airborne Particle Size, Acoustic Airflow and Breathing Pattern on Delivery of Nebulized Antibiotic into the Maxillary Sinuses Using a Realistic Human Nasal Replica, Pharmaceutical Research, (2014) 1-9.
[36] A. Farnoud, I. Baumann, E. Gutheil, Numerical Simulation of the Dispersion and Deposition of a Spray Carried by a Pulsating Airflow in a Patient-Specific Human Nasal Cavity, Atomization and Sprays, 27 (2017) 913-928.
[37] C. Gaberino, J.S. Rhee, G.J. Garcia, Estimates of nasal airflow at the nasal cycle mid-point improve the correlation between objective and subjective measures of nasal patency, Respir Physiol Neurobiol, 238 (2017) 23-32.
[38] A. Fedorov, R. Beichel, J. Kalpathy-Cramer, J. Finet, J.-C. Fillion-Robin, S. Pujol, C. Bauer, D. Jennings, F. Fennessy, M. Sonka, J. Buatti, S. Aylward, J.V. Miller, S.

Pieper, R. Kikinis, 3D Slicer as an image computing platform for the Quantitative Imaging Network, Magnetic Resonance Imaging, 30 (2012) 1323-1341.
[39] Blender2.79.
[40] M. Germano, U. Piomelli, P. Moin, W.H. Cabot, A dynamic subgrid scale eddy viscosity model, Phys Fluids A, 3 (1991) 1760-1765.
[41] J.K. Eaton, Two-way coupled turbulence simulations of gas-particle flows using point-particle tracking, International Journal of Multiphase Flow, 35 (2009) 792-800.
[42] S.B. Pope, Turbulent Flows, Journal of Turbulence, 1 (2000) 771-771.
[43] L. Schiller, A. Naumann, A drag coefficient correlation, Z. Ver. Deutsch. Ing, 77 (1935) 318-320.
[44] M.D. Allen, O.G. Raabe, Slip Correction Measurements of Spherical Solid Aerosol Particles in an Improved Millikan Apparatus, Aerosol Science and Technology, 4 (1985) 269-286.
[45] R. Clift, J.R. Grace, M.E. Weber, Bubbles, Drops, and Particles, Academic Press1978.
[46] J.H.F.a.M. Peric, Computational Methods for Fluid Dynamics, Springer2002.
[47] S.V. Patankar, Numerical Heat Transfer and Fluid Flow, Hemisphere Publishing Corporation1980.
[48] S.V. Patankar, D.B. Spalding, A calculation procedure for heat, mass and momentum transfer in three-dimensional parabolic flows, International Journal of Heat and Mass Transfer, 15 (1972) 1787-1806.
[49] S.V. Patankar, D.B. Spalding, A computer model for three-dimensional flow in furnaces, Symposium (International) on Combustion, 14 (1973) 605-614.
[50] H.K.V.a.W. Malalasekera, An Introduction to Computational Fluid Dynamics, The Finite Volume Method, Prentice Hall2007.
[51] H. Jasak, Error Analysis Estimation for the Finite Volume Method with Applications to Fluid Flows, Imperial College of Science, Technology and Medicine, London, England, 1996.
[52] C.T. Crowe, Multiphase Flow Handbook, CRC Press2006.
[53] D.A. Edwards, J. Hanes, G. Caponetti, J. Hrkach, A. Ben-Jebria, M.L. Eskew, J. Mintzes, D. Deaver, N. Lotan, R. Langer, Large porous particles for pulmonary drug delivery, Science, 276 (1997) 1868-1871.
[54] S.M. Wang, K. Inthavong, J. Wen, J.Y. Tu, C.L. Xue, Comparison of micron- and nanoparticle deposition patterns in a realistic human nasal cavity, Respiratory Physiology and Neurobiology, 166 (2009) 142-151.
[55] D.Y.H. Pui, F. Romay-Novas, B.Y.H. Liu, Experimental Study of Particle Deposition in Bends of Circular Cross Section, Aerosol Science and Technology, 7 (1987) 301-315.
[56] J.T. Kelly, B. Asgharian, J.S. Kimbell, B.a. Wong, Particle Deposition in Human Nasal Airway Replicas Manufactured by Different Methods, Aerosol Science and Technology, 38 (2004) 1063-1071.
[57] J.D. Schroeter, G.J.M. Garcia, J.S. Kimbell, Effects of surface smoothness on inertial particle deposition in human nasal models, Journal of Aerosol Science, 42 (2011) 52-63.
[58] I. Weinhold, G. Mlynski, Numerical simulation of airflow in the human nose, Eur Arch Otorhinolaryngol, 261 (2004) 452-455.
[59] J. Wen, K. Inthavong, J. Tu, S. Wang, Numerical simulations for detailed airflow dynamics in a human nasal cavity, Respir Physiol Neurobiol, 161 (2008) 125-135.

[60] Z. Wang, P.K. Hopke, G. Ahmadi, Y.-S. Cheng, P.A. Baron, Fibrous particle deposition in human nasal passage: The influence of particle length, flow rate, and geometry of nasal airway, Journal of Aerosol Science, 39 (2008) 1040-1054.
[61] M. Breuer, H.T. Baytekin, E.A. Matida, Prediction of aerosol deposition in 90{ring operator} bends using LES and an efficient Lagrangian tracking method, Journal of Aerosol Science, 37 (2006) 1407-1428.
[62] C.J. Tsai, D.Y.H. Pui, Numerical study of particle deposition in bends of a circular cross-section-laminar flow regime, Aerosol Science and Technology, (1990).
[63] L. Nicolaou, T.A. Zaki, Characterization of aerosol Stokes number in 90° bends and idealized extrathoracic airways, Journal of Aerosol Science, 102 (2016) 105-127.
[64] K. Inthavong, A unifying correlation for laminar particle deposition in 90-degree pipe bends, Powder Technology, 345 (2019) 99-110.

There is no conflict of interests between the authors.